nature communications

Article

https://doi.org/10.1038/s41467-024-55107-y

Secondary nucleation guided noncovalent synthesis of dendritic homochiral superstructures via growth on and from surface

Received: 26 July 2024

Accepted: 27 November 2024

Published online: 30 December 2024

Check for updates

Sai Rachana Pramatha[1], Dasari Srideep[1], Udaijit Pattnaik[2], Rahul Sahu[3], Devamrutha Ilayidathu Suresh[2], Aditya Chandrakant Yadav[1,4], Chinmayee Muduli[5], Sandeep K. Reddy[3], Satyaprasad P. Senanayak[2] ✉ & Kotagiri Venkata Rao[1] ✉

Secondary nucleation is an emerging approach for synthesizing higher-order supramolecular polymers with exciting topologies. However, a detailed understanding of growth processes and the synthesis of homochiral superstructures is yet to be demonstrated. Here, we report the non-covalent synthesis of dendritic homochiral superstructures using NIR triimide dyes as building blocks via a secondary nucleation elongation process. Detailed analysis of kinetics and temporal evolution of morphology indicates that the formation of dendritic homochiral superstructures proceeds via growth on the surface and growth from the surface of the seeds. The combination of these two processes leads to the formation of elegant homochiral superstructures with a size of ~0.4 mm^2, having a superhelix at the center and helical fibres as branches. Moreover, these dendritic homochiral superstructures exhibit significantly high chiro-optical photoresponse with the magnitude of g_{factor} reaching a value as high as 0.55 - 0.6. Thus, our results provide insights into the growth process of homochiral superstructures with dendritic topology, which can be critically important for the design and optimization of chiral-selective optoelectronic devices leveraging controlled self-assembly.

Supramolecular polymers (SPs)[1,2] of π-systems find a wide range of applications in the fields of optoelectronics[3–6], catalysis[7,8] and energy storage[9]. SPs form mainly via isodesmic or cooperative (nucleation-elongation) mechanisms, resulting in one-dimensional (1D) chains with high internal order[10–12]. Recent advances in the primary nucleation-elongation process allowed us to synthesize homo[13] and block SPs[14,15] with controlled length and sequence via living supramolecular polymerization (LSP)[16–18]. Despite significant progress in the field of SPs, it is still challenging to synthesize higher-order SP structures[19] using small molecules with precision like that of covalent polymers[20,21]. Controlling the topology of SPs is crucial to attain new properties and functions as seen in covalent polymers[22,23]. Moreover, many bio-systems possess

[1]Department of Chemistry, Indian Institute of Technology Hyderabad, Kandi, Sangareddy, Telangana, India. [2]Nanoelectronics and Device Physics Lab, School of Physical Sciences, National Institute of Science Education and Research (NISER), Bhubaneswar, OCC of HBNI, Jatni, Khurdha, Odisha, India. [3]Centre for Computational and Data Science, Indian Institute of Technology Kharagpur, Kharagpur, West Bengal, India. [4]Department of Materials Science and Metallurgical Engineering, Indian Institute of Technology Hyderabad, Kandi, Sangareddy, Telangana, India. [5]ICAR-Central Institute of Freshwater Aquaculture, Bhubaneswar, India. ✉e-mail: satyaprasad@niser.ac.in; kvrao@chy.iith.ac.in

unique topologies formed via hierarchical assembly[24,25]. Although Winnik and Manners et al. demonstrated the synthesis of various higher-order supramolecular assemblies with high precision[26–28] via living crystallization-driven self-assembly of polymer building blocks, it is still challenging with small molecules. In the case of LSP via a primary nucleation event, elongation takes place at the active ends of the seeds and the resultant morphology is the same as the seeds but with increased dimensions[16–18]. Hence, LSP via primary nucleation could yield only 1D or 2D SPs with controlled dimensions[18,29]. In this context, surface-catalyzed secondary nucleation event, a mechanism that is well explored in protein assemblies plays a pivotal role in the synthesis of SPs with higher-order topologies[30,31]. The utilization of secondary nucleation mechanisms for synthesizing higher-order supramolecular assemblies using small molecules just began to appear[32–34]. For example, Yagai et al.[33] demonstrated the synthesis of supramolecular nano-polycatenanes using hydrogen-bonded (H-bonded) rosette assemblies. In another report, Sugiyasu et al.[34] achieved the synthesis of Archimedean spirals using H-bonded porphyrins. We have recently reported the synthesis of 3D spherical spherulites and scarf-like SP heterostructures using perylene diimides via a secondary nucleation-elongation process[35].

Chirality is an important aspect of self-assembled structures such as SPs[36,37] and polymer assemblies[38–41]. The study of chiral supramolecular assemblies helps us to understand the origin of homochirality in nature. Chiral assemblies are utilized for circularly polarized luminescence[38–42], asymmetric catalysis[37,43], biomedical applications[44] and electron-spin filtering applications[45]. Several elegant molecular designs are reported for the synthesis of 1D chiral assemblies with single[36] or double[46] or superhelical structures[47–49]. However, rational design principles for the synthesis of chiral supramolecular assemblies with hierarchical topologies are seldom reported[50,51]. Although the synthesis of higher-ordered chiral assemblies is well executed in biological systems[52], it is still a major challenge for synthetic systems. Recently, George et al. achieved stereoselective induction of secondary nucleation pathways with chiral monomers[53]. However, higher-ordered chiral assemblies could not be achieved due to the detachment of SPs from the surface of the seed. To overcome this, phenyl groups containing tripeptide side chains were introduced to stabilize the SP on the seed surface. However, the growth is restricted only across the length of the seed[54]. Hence, the non-covalent synthesis of higher-ordered chiral assemblies, reminiscent of biological systems, remains a grand challenge[52]. Thus, a deeper understanding of molecular designs and the growth process are indeed important for further development in this field and the controlled synthesis of higher-order chiral SPs as they are capable of showing outstanding chiroptical functions[55–58].

Herein, we present an important advancement in this field for the synthesis of higher-order chiral SP architectures of π-conjugated molecules having dendritic topology via secondary nucleation. This is demonstrated using NIR-absorbing triimide dyes substituted with chiral alkyl chains (***S*-G** and ***R*-G**) (Fig. 1a). Although these NIR dyes have been known for a long time, they have not yet been explored for supramolecular polymerization[59]. The presence of donor groups and a phenyl ring at the bay position not only provides NIR absorption but also significantly enhances their stacking efficiency and order compared to the corresponding perylene diimides (PDIs)[35,60]. Interestingly, in 15 vol% $CHCl_3$ (good solvent) in isopropanol (IPA, poor solvent), ***S*-G** and ***R*-G** display temporal evolution of morphology. With time, these molecules evolve into macroscopic dendritic homochiral superstructures (DHS) having a size of ~0.4 mm^2 with an expression of macroscopic chirality (Fig. 1b). Detailed electron microscopy studies and kinetic analysis reveal that the formation of these higher-order chiral architectures take place via a secondary nucleation-elongation mechanism (Fig. 1b). Our investigations reveal that a few monomers are initially converted into short 1D chiral SPs through primary nucleation. Next, the remaining monomers in the solution nucleate and elongate 'on the surface' as well as 'from the surface' of the 1D chiral SP seeds (Fig. 1b). The repetition of these two processes results

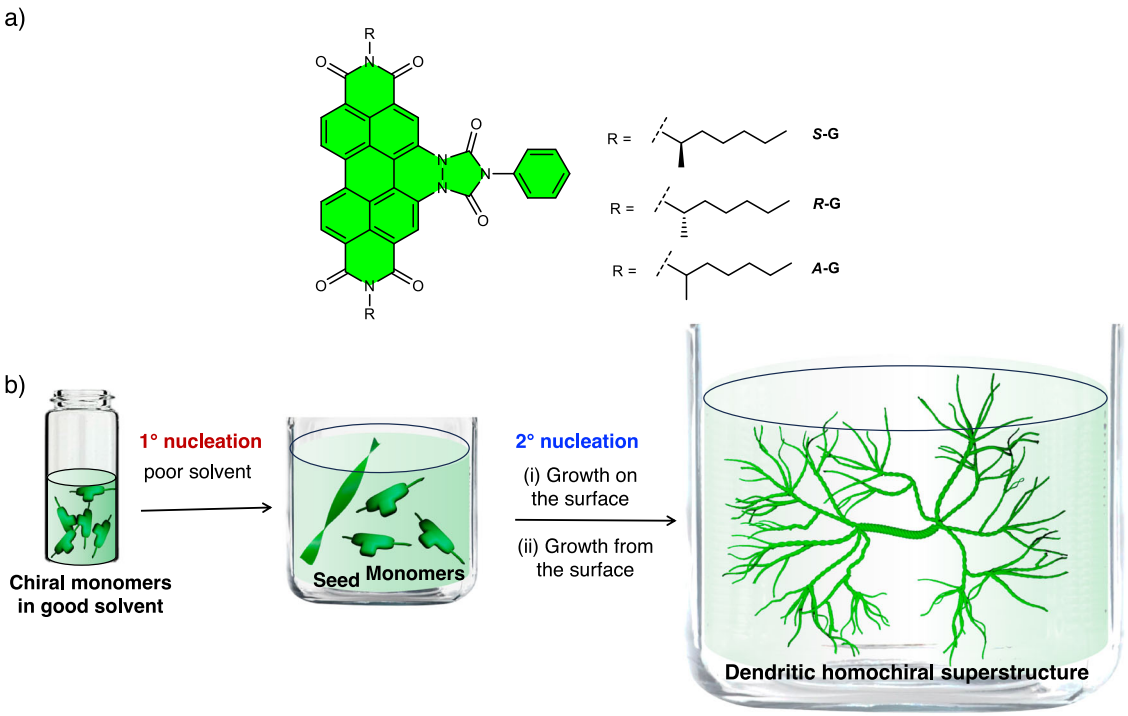

Fig. 1 | Molecular structures and summary of the formation of dendritic homochiral superstructures (DHS). a Molecular structures of NIR triimides having chiral (***S*-G** and ***R*-G**) and achiral alkyl (***A*-G**) side chains. **b** schematic illustration of the formation of dendritic homochiral superstructures via 'growth on the surface' and 'growth from the surface' secondary nucleation-elongation process. The schematic has been made using Blender 3.5 software.

https://doi.org/10.1038/s41467-024-55107-y

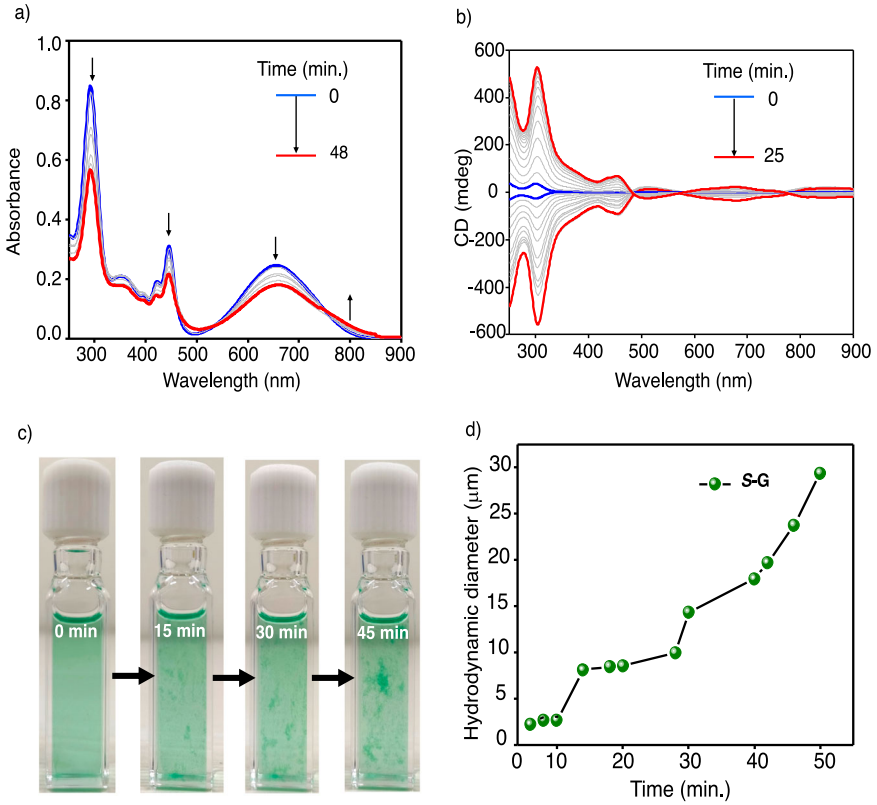

Fig. 2 | Probing the temporal evolution of supramolecular polymers. a Time-dependent absorption spectra of 30 μM solution of ***S*-G** in 15% $CHCl_3$ in IPA over a period of 48 min. representing its temporal growth. **b** Time-dependent CD spectra of a 30 μM solution of ***S*-G** and ***R*-G** in 15% $CHCl_3$ in 85% IPA. **c** Photographs of solution of ***S*-G** (30 μM) in 15% $CHCl_3$ in IPA at different time intervals. **d** Time-dependent dynamic light scattering (DLS) data of ***S*-G** (30 μM) in 15% $CHCl_3$ in IPA.

in the formation of DHS composed of a thick central superhelix and branches of thin 1D helical fibers. Under similar conditions, the corresponding PDIs do not self-assemble, and the achiral triimide dye (***A*-G**) forms only 1D fibers, thus highlighting the importance of bay substitution and chiral side chains in the formation of DHS (Fig. 1). The temporal evolution of SPs into DHS and their interaction with circularly polarized light is also probed to understand the enhancement in the chirality with self-assembly. It was possible to follow the growth of the self-assembled structure with the variation in optoelectronic properties. Interestingly, the temporal evolution of DHS results in an enhancement of conductivity by at least two to three times. Moreover, the DHS exhibits a clean selective chiro-optical response in the solution phase with a magnitude of g_{factor} ~ 0.55–0.61 and responsivity as high as 2 mA/W, which is among the best for supramolecular semiconductors. Nevertheless, these measurements indicate that electrical measurements can be a way to probe supramolecular self-assembly while, at the same time, the differential photoresponse to left and right circularly polarized light highlights the potential of such programmable structures for applications in circularly polarized light detection and chiroptical devices.

Results and discussion

The molecules under investigation, ***S*-G, *R*-G** and ***A*-G** were synthesized from respective PDIs (Fig. 1 and Supplementary Fig. 1). The detailed synthetic procedure is given in the supplementary information (Supplementary Note 2). From these PDIs (Supplementary Figs. 2–4), respective NIR dyes, ***S*-G, *R*-G** and ***A*-G** were synthesized in an efficient one-step oxidative Diels-Alder reaction[59]. The desired product was isolated, purified, and characterized using various analytic techniques (Supplementary Figs. 5–17). Thermogravimetric analysis reveals that all three triimide dyes are thermally stable up to 350 °C (Supplementary Fig. 17). The UV-Vis spectrum of ***S*-G** in $CHCl_3$ (30 μM) solution at 25 °C shows absorption peaks ranging from 250 nm to 800 nm, with three distinct regions and absorption maxima at 300 nm (Supplementary Fig. 19a). The appearance of a broad peak from 500 nm to 800 nm is due to the introduction of bay substitution in PDI, which facilitates intramolecular charge transfer. Well-resolved vibronic features are observed between 390 nm and 460 nm[59]. These features indicate the molecularly dissolved state of ***S*-G** (30 μM) in $CHCl_3$. We investigated the supramolecular polymerization behavior of a 30 μM solution of ***S*-G** by varying the solvent percentage of $CHCl_3$ and IPA while probing its absorption and emission spectra. As the vol% of IPA increases in $CHCl_3$, a decrease in the absorbance of all the peaks and broadening of the peak between 500 nm to 800 nm and the appearance of weak red-shifted absorbance around 800 nm was observed (Supplementary Fig. 19a). Moreover, the loss of vibronic features of the peaks from 390 nm to 460 nm was also clearly evident from the absorption spectra. Simultaneously, it has been noted that the molecularly dissolved state in $CHCl_3$ is fluorescent, with a λ_{max} ~768 nm, but upon an increase in vol% of IPA, the fluorescence emission is completely quenched (Supplementary Fig. 19b). These features can be attributed to the supramolecular polymerization of ***S*-G** with face-to-face stacking (vide infra). As expected, the molecularly dissolved solution of ***S*-G** (30 μM) is CD silent (Supplementary Fig. 19c). For the solutions having ***S*-G** (30 μM) in 85, 90 and 95 vol% of IPA in $CHCl_3$, a strong CD signal is observed due to the transfer of chirality from the chiral alkyl side chains to the core of ***S*-G** upon supramolecular polymerization.

Interestingly, the freshly prepared solutions of ***S*-G** (30 μM) in 15% $CHCl_3$ in IPA started to show further changes in the absorption spectra over a period of 48 min. at 25 °C (Fig. 2a). With time, a gradual decrease of all absorption bands, along with a further increase in absorbance

https://doi.org/10.1038/s41467-024-55107-y

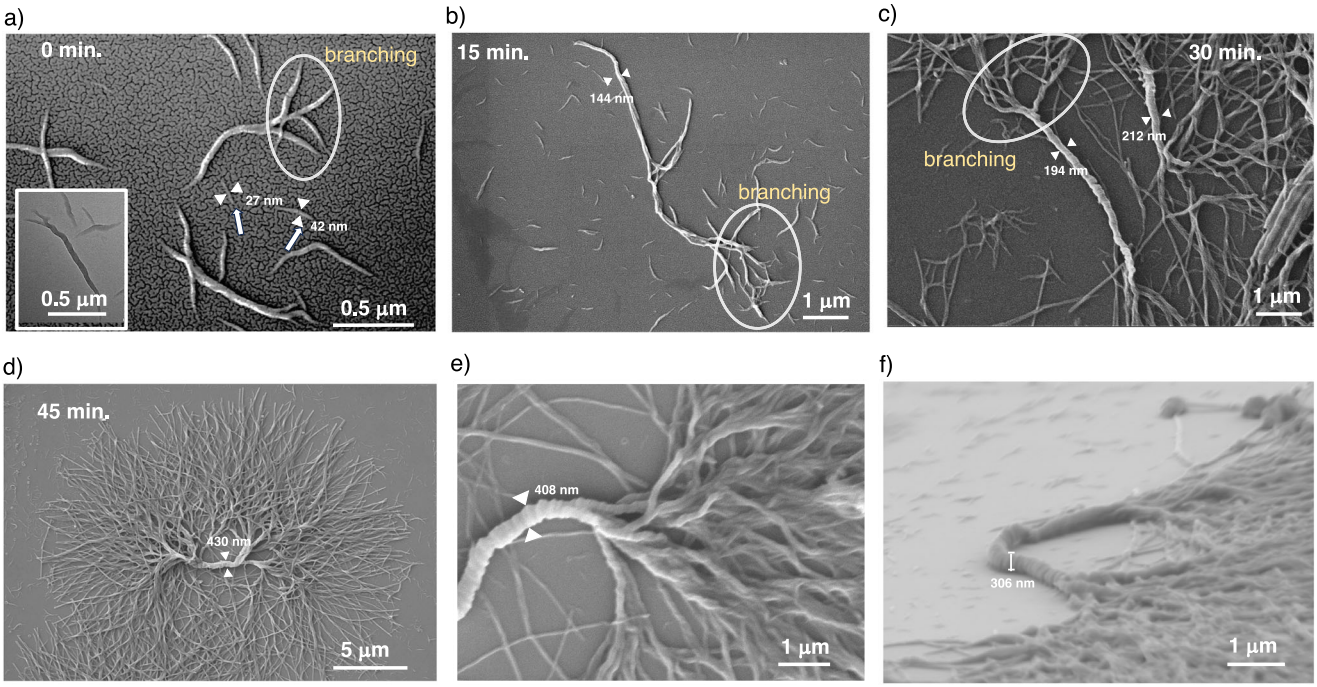

Fig. 3 | Probing the evolution of supramolecular polymers into dendritic homochiral superstructures (DHS) using FE-SEM. Field-emission scanning electron microscopy (FE-SEM) images of ***S*-G** (30 µM) in 15% $CHCl_3$ in IPA spin-coated on a silicon wafer at various time intervals. **a** At 0 min., freshly prepared aggregates are smaller in size, consisting of single and double helices, white arrows show primary nucleation fibers, and circled areas indicate branching (inset: transmission electron microscopy (TEM) image showing a double helix formation). **b** After 15 min., intertwined helices grow bigger in length and width with increased branching. **c** After 30 min., the intertwined helices start forming a superhelix of widths between 190 nm to 220 nm and with further increased branching. **d** After 45 min., we observed dendritic homochiral superstructures (DHS) having a superhelix of width 430 nm with extensive branching. **e** A magnified FE-SEM image of the central superhelix from which smaller helices are originating shows that the superhelix is composed of multiple helices. **f** A 3D image of DHS showing a superhelix core with a height of ~305 nm.

around 800 nm was observed (Fig. 2a). Moreover, the peaks from 390 nm to 460 nm became further broad (Fig. 2a). These observations indicate that further assembly of ***S*-G** with time in solution. Along with the changes in the absorption spectra, the CD spectra also showed a further increase in the signal over time (Fig. 2b). In the case of ***S*-G**, a weak CD signal is obtained for the freshly prepared solution having a small positive cotton effect at 300 nm. The initially low-intense CD signals become more intense, with further progress in self-assembly peaking nearly at 25 min. (Fig. 2b and Supplementary Fig. 20). Similar behavior was obtained during the aggregation of ***R*-G**. Moreover, a mirror image relation in CD spectra is seen for the temporal aggregation of ***S*-G** and ***R*-G** (Fig. 2b). The freshly prepared solution of ***S*-G** (30 µM) in 15% $CHCl_3$ in IPA is visibly clear but emerged as a green suspension in nearly 45 min. (Fig. 2c). As a result, a reduction in the CD signal after 25 min. was observed due to the crashing of self-assembled structures out of the solution. These observations suggest the formation of higher-ordered SPs of NIR dyes with time. We have also performed time-dependent linear dichroism (LD) measurements to understand its contribution to the CD signal and preferential orientation of SPs in solution. Although the LD signal is weak, we have seen a significant increase after 5 min. and saturation after 25 min. (Supplementary Fig. 21). Hence, the contribution of the LD signal to the CD signal is low, and the resultant SPs have some degree of preferential orientation in the solution. To validate this temporal hierarchical self-assembly process further, we have carried out a time-dependent DLS study by which we could monitor the growth in the size of aggregates (Fig. 2d). With time, an increase in hydrodynamic diameter is seen, establishing that a time-dependent self-assembly growth is underway. In 48 min., the hydrodynamic radius of the assemblies is increased from 2.0 µm to 30 µm.

In order to gain insights into the morphological evolution of ***S*-G** with time, we performed field-emission scanning electron microscopy (FE-SEM) by spin-coating the solutions onto a silicon wafer substrate at different time intervals. It is observed that a freshly prepared solution of ***S*-G** in 15% $CHCl_3$ in IPA showed the presence of small helical fibers and a few double helices of less than 1 µm in length and width ranging from 27 nm to 42 nm (Fig. 3a). This is further supported by transmission electron microscopy (TEM) images as well (Supplementary Fig. 22). Interestingly, we have also observed a few fibers having branches and higher thicknesses (Fig. 3a). After 15 min., the morphology grew into multiple intertwined helices along with increased branching to dimensions >5 µm in length and nearly 140 nm to 150 nm in width (Fig. 3b). After 30 min., the appearance of a thick superhelix, along with several small helical fiber branches, is seen. The width of the superhelix is between 190 nm to 220 nm, and the length of each branched structure is >10 µm (Fig. 3c). After 45 min., we found the formation of DHS with extensive branching covering an area of 0.4 mm^2 bearing a central superhelix having a width greater than 400 nm (Fig. 3d). A closer look at the image of the central superhelix reveals that it is composed of multiple intertwined helices that segregate at the ends into smaller bunches of helices and ultimately into helical fibers (Fig. 3e). A 3D image of the DHS was obtained by tilting the sample at 72°, showing the superhelix's height to be >300 nm (Fig. 3f). Further analysis of FE-SEM and atomic force microscopy (AFM) images revealed that the central superhelix and branched thin helical fibers formed from ***S*-G** have a right-handed helical orientation (Supplementary Fig. 23). Similarly, FE-SEM and AFM images revealed the left-handed helical orientation for DHS formed from of ***R*-G** (Supplementary Fig. 24). These observations not only confirm the opposite helicity of DHS formed from ***S*-G** and ***R*-G** but also their homochiral nature.

Next, to understand the role of chiral side chains and bay substitution in the formation of DHS, we have investigated the supramolecular polymerization of ***A*-G** and ***S*-PDI**. First to understand the role of chiral side chains, we have synthesized ***A*-G** using commercially available racemic 2-heptylamine. Like ***S*-G** and ***R*-G**, a 30 μM solution ***A*-G** also showed temporal evolution of SPs in 15% $CHCl_3$ in IPA (Supplementary Fig. 25a, b). However, the resultant morphology is 1D fibers, not DHS, as evidenced by FE-SEM images (Supplementary Fig. 25d, e). As expected, the CD signal of SPs of ***A*-G** is negligible due to the achiral nature of the resultant SPs (Supplementary Fig. 25c). This indicates that chirality in the side chain is crucial to form DHS. Next, to understand the role of bay substitution, we have investigated the supramolecular polymerization of ***S*-PDI**. We found that a 30 μM solution of ***S*-PDI** in 15% $CHCl_3$ in IPA exists as a monomer even after keeping it at 25 °C for 14 h (Supplementary Fig. 26a). This indicates the weak-stacking efficiency of ***S*-PDI** compared to ***S*-G**. At higher concentrations, such as 200 μM, ***S*-PDI** formed self-assembled structures (Supplementary Fig. 26b) with needles-like morphology after keeping for 3 h at 25 °C (Supplementary Fig. 26c). Hence, both chirality in the side chain and bay substitution are important for the formation of DHS.

To further understand the role of the bay substitution in improving the stacking efficiency of NIR dyes (***S*-G** and ***R*-G**), we have performed theoretical calculations on both dimers and a stack consisting of 24 monomers in 15% $CHCl_3$ in IPA solvent mixture (Supplementary Note 4). Gas-phase quantum mechanical calculations revealed that the intermolecular interaction energy between ***S*-G** monomers is approximately 60 kJ/mol higher than that of the ***S*-PDI** monomers, demonstrating that the ***S*-G** dimer is more stable. Energy decomposition analysis indicated that the bay substitution enhances the stability of the ***S*-G** dimer by considerably strengthening the electrostatic, dispersion, and charge transfer interactions (Supplementary Fig. 27). In contrast, the absence of bay substitution in ***S*-PDI**s results in their self-assembly at relatively higher concentrations, primarily due to their weaker intermolecular interactions compared to those of ***S*-G** molecules. To further investigate the influence of solvent on the stacking propensity and orderliness in the extended fiber, we conducted all-atom classical molecular dynamics simulations on preformed stacks in an explicit solvent mixture of 15% $CHCl_3$ in IPA. The presence of strong peaks in the radial distribution function (g(r)) of both systems indicates that both ***S*-G** and ***S*-PDI** stacks are stable in solution (Supplementary Fig. 28)[61]. Importantly, the intensity of the first peak is higher for ***S*-G**, suggesting a greater stacking propensity than ***S*-PDI** stacks. The g(r) calculated from the extended trajectory (200–300 ns), reveals the emergence of long-range order in the structures of ***S*-G** compared to ***S*-PDI** (Supplementary Fig. 28b). This is due to the phenyl rings exhibiting dynamic behavior, tending to adopt a slanted orientation with an average angle of approximately ±25° relative to the aromatic core (Supplementary Fig. 28e). As a result, several additional non-covalent interactions are favored in the ***S*-G** stack, such as π-π interactions between neighboring phenyl rings, CH-π interactions between adjacent phenyl rings and CH-π interactions between the branched methyl group of one molecule and the phenyl ring of a neighboring molecule (Fig. 4a). Thus, the bay substitution in the ***S*-G** enhances the ordering and stabilization of its SPs compared to the ***S*-PDI**, while the chiral side chains provide the bias for supramolecular chirality, resulting in the formation of DHS (See Supplementary Figs. 27 and 28 and further explanation there).

A lag phase in the temporal aggregation indicates the presence of secondary nucleation events in the formation of DHS. To get further insights, we have analyzed the kinetic profiles of hierarchical assemblies at different monomer concentrations such as 15 μM, 20 μM, 25 μM, 30 μM and 35 μM (Fig. 4b, c). We found that 15 μM is the threshold concentration because, at 10 μM, no significant changes in the absorption spectra were observed even for 3 h at 25 °C (Supplementary Fig. 29). Above 35 μM, such as 40 μM, temporal self-assembly is rapid. Hence, we have analyzed the growth kinetics for five different concentrations (15 μM to 35 μM) by monitoring the absorbance at 650 nm wavelength. The decrease in absorbance at 650 nm indicates the supramolecular polymerization of ***S*-G** (Figs. 2a, 4c). Figure 4c shows the plot of the degree of supramolecular polymerization (α @650 nm) versus time at various concentrations of ***S*-G**. With the decrease in the concentration of ***S*-G**, an increase in half-time of supramolecular polymerization is observed. At 35 μM, the half-time is 550 sec. which increased to >3550 sec. by decreasing the concentration to 15 μM (Fig. 4c). The double logarithmic plot between the log of half-time and the log of concentration gives the value of slope (also known as γ value or scaling exponent value) as −2.264 (Fig. 4b). This value was obtained by using amylofit software (http://www.amylofit.ch.cam.ac.uk) developed by Knowles and group[62]. The scaling exponent value is indicative of the dependence of aggregation kinetics on the monomeric concentration. The absence of curvature in the linear fit suggests that it should align well with the secondary nucleation mechanism[53,62]. Given the relation between scaling exponent (γ) and secondary nucleation order n_2, that comes out to be 4, and n_c comes out to be 3. In this case, the best fit with MSE (mean square error) less than 0.00162 is obtained in secondary nucleation, dominated and unseeded (Fig. 4c and Supplementary Table 1). An ill-fit is obtained for the primary nucleation-elongation model with greater MSE (Supplementary Fig. 30 and Supplementary Table 1). Thus, we conclude that the formation of DHS is aided by a surface-assisted secondary nucleation phenomenon.

The detailed time-dependent microscopic and kinetic analysis revealed that the rapid addition of poor solvent (IPA) to the monomers in $CHCl_3$ leads to the conversion of some of the monomers into short 1D helical SPs via a primary nucleation event[63] (Figs. 3a, 5 and Supplementary Fig. 19). With time, we have seen a further decrease in monomer concentration and an increase in the width of fibers and branching. This indicates that the short 1D helical SPs formed via a primary nucleation event act as seeds for the secondary nucleation events. The increase in the width and length suggests that the remaining monomers in the solution nucleate and elongate on the surface of the short 1D helical SP seeds. This 'growth on the surface' first leads to the formation of a double helix (Figs. 3a, 5). The monomers also nucleate from the surface of the seeds to result in branching as evidenced by FE-SEM images (Figs. 3a, 5)[64]. The remnant monomers in the solution now assemble via 'growth on the surface' to contribute to the formation of a superhelix core and 'growth from the surface' leads to extensive branching (Figs. 3b–d and 5). The branched fibers also exhibit the formation of intertwined helices due to growth on their surface and further undergo branching from the surface to give extensive helical branched structures (Fig. 3e). This interplay of 'growth on the surface' and 'growth from the surface,' via secondary nucleation event eventually leads to the formation of final DHS (Figs. 3 and 5).

Next, we investigated the role of solvent percentage on the formation of DHS. At 20 vol% of $CHCl_3$ in IPA, no significant change leading to the hierarchical self-assembly of ***S*-G** was observed, as evidenced by the absorbance versus time plot monitored at 650 nm wavelength (Fig. 6a). Upon increasing the poor solvent (IPA) to 85% (15% $CHCl_3$), the self-assembly process is completed in 48 min., giving DHS (Figs. 3e, 4b, 6b and Supplementary Fig. 31a, b). The hierarchical self-assembly process was completed more quickly by further increasing the IPA vol% to 90 and 95 in $CHCl_3$.When the IPA is 90%, we have observed the formation of superhelix with less branching and smaller widths (~170 nm to 185 nm) (Fig. 6c and Supplementary Fig. 31c, d). At 95% IPA (5% $CHCl_3$), the self-assembly of ***S*-G** was completed in less than a min., but no evidence of DHS and mostly 1D superhelical fibers with very little branching was observed (Fig. 6d and Supplementary Fig. 31e, f). The increase in vol% of poor solvent (IPA) to

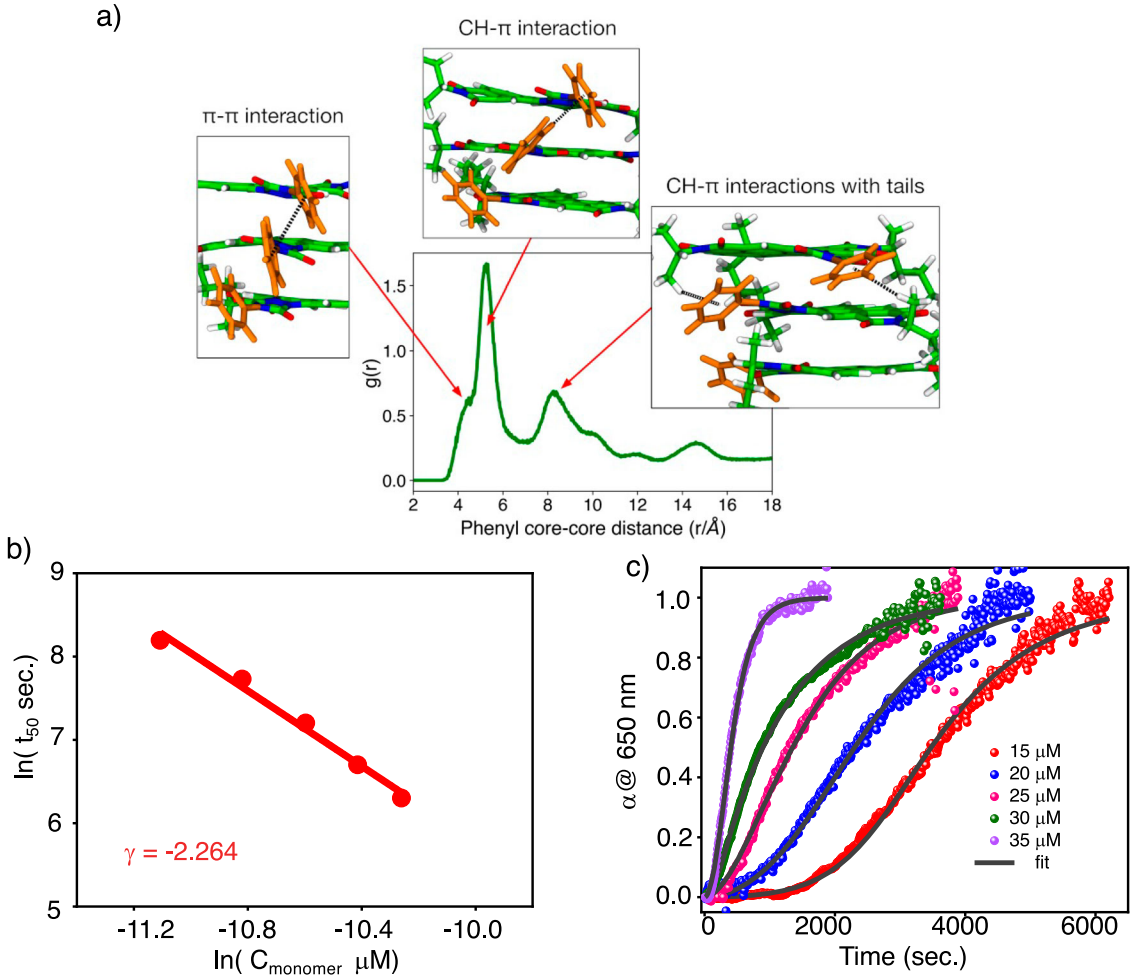

Fig. 4 | Importance of bay substituted phenyl ring and kinetic analysis of self-assembly. a The radial distribution functions (RDF), g(r), between geometric center of phenyl rings in ***S*-G** stack. The phenyl rings are observed to engage in three distinct types of interactions within the ***S*-G** stack: first, π-π interactions between neighboring phenyl rings, corresponding to the shoulder at 4.3 Å in the g(r); second, CH-π interactions between adjacent phenyl rings, leading to the peak at 5.2 Å; and third, CH-π interactions between the branched methyl group of one molecule and the phenyl ring of a neighboring molecule, resulting in the peak at 8.2 Å. **b** Double logarithmic plot of concentration and half-time of ***S*-G** at concentrations of 15 μM, 20 μM, 25 μM, 30 μM and 35 μM showing a linear fit. The slope gives the value of scaling exponent (γ) to be −2.264. **c** Kinetic profiles of aggregation of 15 μM, 20 μM, 25 μM, 30 μM and 35 μM solutions in 15% $CHCl_3$ in IPA and corresponding fit in secondary nucleation dominated-unseeded, shows increasing lag time with decreasing concentration of ***S*-G**. Here α @650 nm represents the degree of supramolecular polymerization monitored at 650 nm.

90 and 95, increases the number of seeds available for the growth of monomers compared to 85 vol% of IPA. This is further evidenced by the lower absorbance at 650 nm at zero min. (Fig. 6a). Due to the increased seed percentage with respect to monomers in the solution, the secondary nucleation and elongation process becomes rapid with shorter half-time for the solutions having 90 and 95 vol% IPA in $CHCl_3$. As a result, the growth process is completed quickly before leading to the formation of DHS. The formation of mostly 1D superhelical fibers in 95 vol% IPA in $CHCl_3$ indicate that the secondary nucleation and elongation process is mainly dominated by growth on the surface (Figs. 5 and 6d). These observations further prove that to achieve dendritic topology, secondary nucleation and elongation via growth from the surface are crucial.

We have also investigated the effect of temperature on DHS formation and depolymerization into monomers. At 25 °C, for a 30 μM solution of ***S*-G** in 15% $CHCl_3$ in IPA, DHS were obtained in 48 min. When cooled to lower temperatures, such as 15 °C, the assembly became rapid and completed in <30 min. (Supplementary Fig. 32a, c). However, the DHS obtained were smaller in size (Supplementary Fig. 32c). At higher temperatures such as 30 °C, even after 3 h, no significant decrease in absorbance at 650 nm, indicating that DHS formation is hampered (Supplementary Fig. 32a, b). Even after 6000 sec., very little decrease in the absorbance is seen (Supplementary Fig. 32b). To understand whether ***S*-G** in 15% $CHCl_3$ in IPA can be completely depolymerized into monomers, a freshly prepared 30 μM solution of ***S*-G** in 15% $CHCl_3$ in IPA was heated to 65 °C. Although absorbance is increased compared to that of at 25 °C, but could not reach like monomers in pure $CHCl_3$, indicating incomplete depolymerization into monomers even at 65 °C (Supplementary Fig. 33a, d). We could not go beyond 65 °C due to the evaporation of $CHCl_3$. When this solution is cooled back to 25 °C, the absorption spectrum obtained is similar to the freshly prepared solution at 25 °C. After allowing it at 25 °C for 48 min., the formation of DHS was observed, as evidenced by the FE-SEM images (Supplementary Fig. 33a, e). We have also tried the 15 μM solution of ***S*-G** in 15% $CHCl_3$ in IPA, but complete depolymerization into monomers is not observed at 65 °C (Supplementary Fig. 33b). Similarly, after the formation of DHS (30 μM), the solution was heated at 65 °C, but complete depolymerization was not observed (Supplementary Fig. 33c). When this hot solution was spin-coated on a silicon wafer and visualized using FE-SEM, short helical fibers were observed (Supplementary Fig. 33f). This indicates that in 15% $CHCl_3$ in IPA at 65 °C, DHS can be dissociated into short helical fibers but not

https://doi.org/10.1038/s41467-024-55107-y

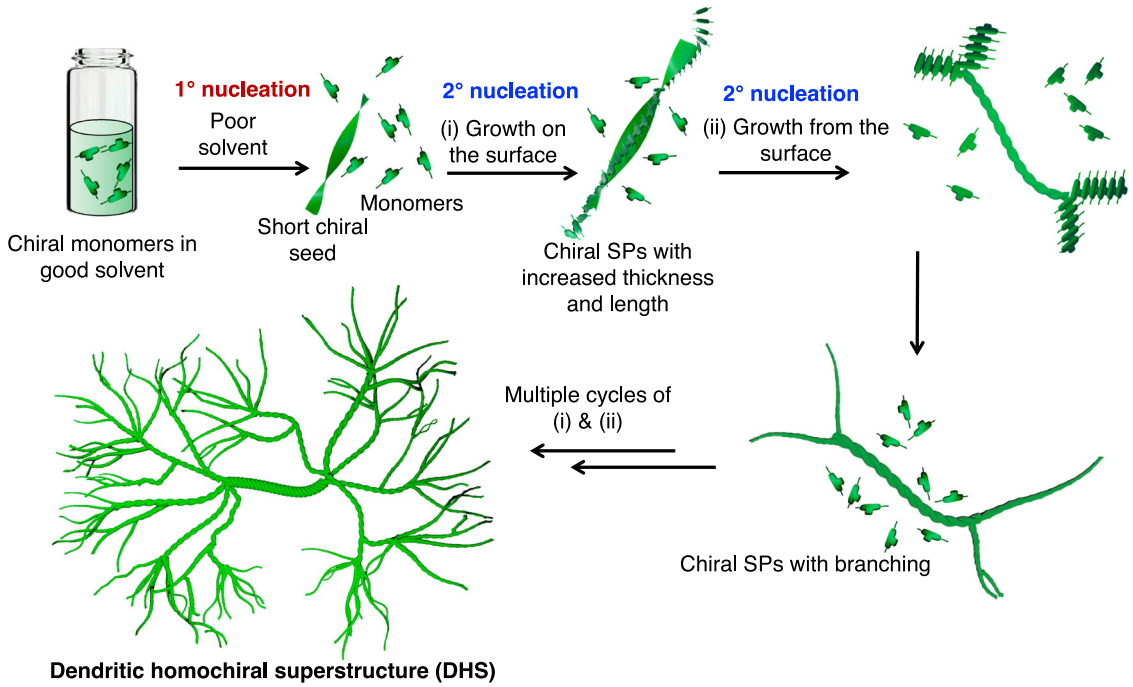

Fig. 5 | Schematic illustration of DHS formation. Schematic illustration of the formation of dendritic homochiral superstructures (DHS) via 'growth on the surface' and 'growth from the surface' of the seeds via secondary nucleation-elongation mechanism. The schematic has been made using Blender 3.5 software.

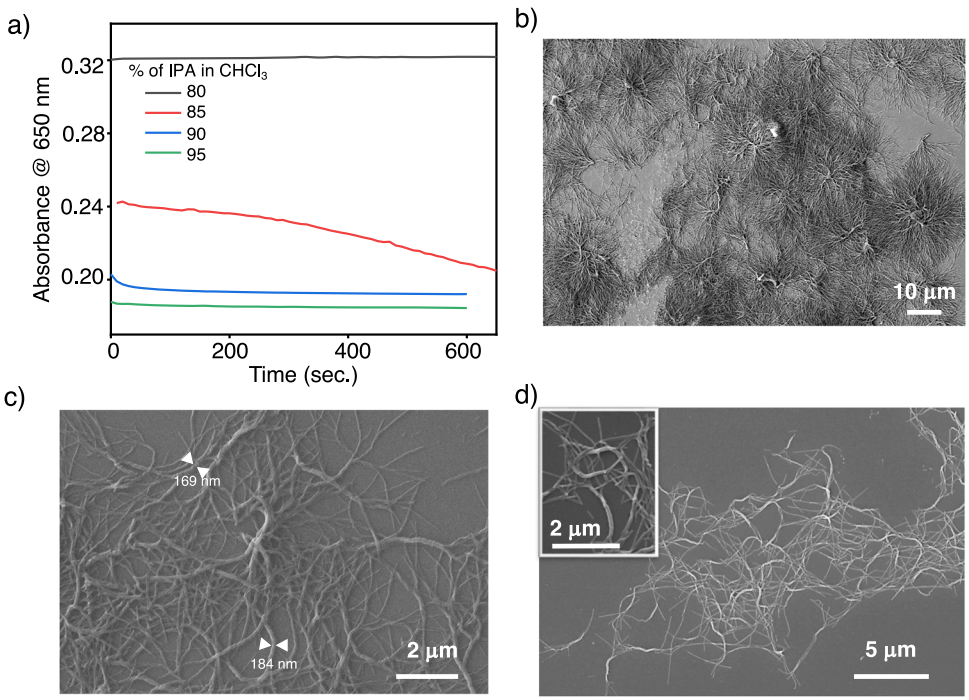

Fig. 6 | Effect of solvent composition on dendritic homochiral superstructures (DHS) formation. a Time-dependent variation in the absorbance of ***S*-G** (30 µM) at various volume % of IPA in $CHCl_3$ monitored at 650 nm. Field-emission scanning electron microscopy (FE-SEM) images of a 30 µM solution of ***S*-G** (**b**) in 15% $CHCl_3$, (**c**) 10% $CHCl_3$ and (**d**) 5% $CHCl_3$ in IPA, spin-coated onto a silicon wafer. The inset of **d** shows the enlarged FE-SEM image of superhelices with very little branching.

completely into monomers. When the DHS solution was sonicated for 15 min., they were also not fully depolymerized into monomers, as evidenced by the absorption spectra, but fragmented into superhelix and helical fibers (Supplementary Fig. 34).

To understand how the DHS formation will be affected by mixing different molar ratios of ***S*-G** and ***R*-G**, we have mixed them in their monomeric state in $CHCl_3$ in 1:1, 1:2 and 1:5 molar ratios before adding IPA (Supplementary Fig. 35). The growth of the SPs has been monitored using CD spectroscopy and FE-SEM imaging. The equimolar mixture of ***S*-G** and ***R*-G** has negligible CD signal compared to homochiral aggregates, and it is similar to ***A*-G** (Supplementary Figs. 25c and 35a). FE-SEM images obtained after completion of the self-assembly process revealed the existence of 1D fibers similar to ***A*-G** but not DHS (Supplementary Fig. 35d, g). When the ratio of ***R*-G** to ***S*-G** is changed to

https://doi.org/10.1038/s41467-024-55107-y

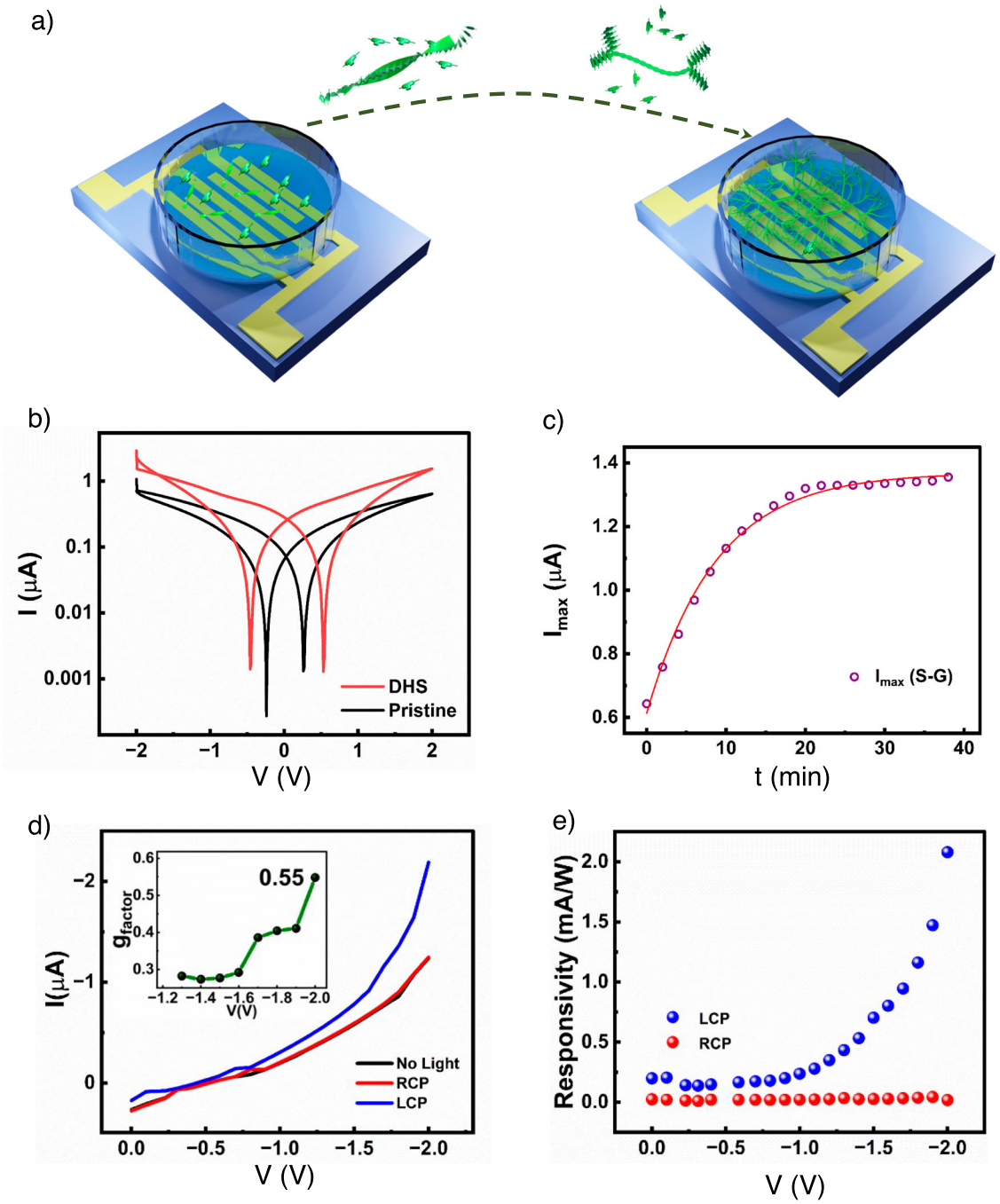

Fig. 7 | Chiro-optical response of dendritic homochiral superstructures (DHS) in solution. a Schematic representation of device structure utilized for the time-dependent I–V measurements in solution. The schematic has been made using Blender 3.5 software. **b** I–V characteristics of ***S*-G** in 15% $CHCl_3$ in IPA mixture at 0 min. (pristine) and after 50 min. (DHS). **c** Temporal evolution of I_{max} for the solution of ***S*-G**. **d** Photocurrent generated upon illumination of ***S*-G** with left circularly polarized (LCP) and right circularly polarized (RCP) light. The inset shows the variation of g_{factor} with voltage. **e** Estimation of photoresponsivity upon illumination of ***S*-G** solution with LCP and RCP.

1:2 (10 μM of ***R*-G** and 20 μM of ***S*-G**) and 1:5 (5 μM of ***R*-G** and 25 μM of ***S*-G**), the CD signals obtained are slightly lower than pure ***S*-G** (Supplementary Fig. 35b, c). The FE-SEM analysis of these samples indicated the presence of chiral SPs with branches, and DHS with less branching, but not fully developed DHS as seen in the case of pure ***S*-G** (Supplementary Fig. 35e, f, h, i). Multiple areas were analyzed to identify homochirality, and it was concluded that these helices are right-handed similar to SPs obtained from ***S*-G**. Hence, we conclude that fully developed DHS can be synthesized via secondary nucleation using pure chiral isomers (***S*-G** or ***R*-G**).

The temporal evolution of NIR-absorbing ***S*-G** and ***R*-G** into higher-ordered SP architectures such as DHS further motivated us to investigate the variation of electrical properties with the evolution in morphology. For this purpose, a custom-designed 2 mL hollow chamber was securely attached using silicone adhesive over a patterned Cr/Au electrode channel fabricated on glass substrates (Fig. 7a and Supplementary Fig. 36). A 30 μM solution of ***S*-G** in 15% $CHCl_3$ in IPA is placed in the hollow chamber, and time-dependent I–V characteristics are recorded in the solution phase (See methods section). Typical time-dependent I–V characteristics are depicted in Supplementary Fig. 37.

The self-assembly process begins from small helical fibers (pristine sample, 0 min.) and finally evolve into DHS over a period of 50 min. (Fig. 7a). Interestingly, the channel current increases monotonously from 0.6 μA to 1.4 μA for ***S*-G** samples (a similar level of enhancement in current was also observed in ***R*-G** samples) as the self-assembly proceeds from small helical fibers to DHS (Fig. 7b and Supplementary Fig. 37). This temporal evolution of I_{max} (maximum current at 2 V) followed an exponential growth (Fig. 7c and Supplementary Fig. 37a). These observations further indicate that DHS show more than two times enhancement in channel current than the initial short helical fibers. It is worth noting that the temporal evolution of the I–V characteristics is consistent with the temporal evolution observed from electronic absorption and CD measurements (Fig. 2a, b) in the solution phase, indicating a general internal consistency within the results.

Reports on the successful use of chiral π-conjugated molecules in chiroptical sensors[55–58] have spurred interest in exploring the potential of our DHS for similar applications. These reports highlight the ability of π-conjugated molecules to exhibit unique chiro-optical properties, which can be harnessed for sensitive and selective detection of left and right circularly polarized light. Hence, we further explored the chiro-optical response of both ***S*-G** and ***R*-G** solutions while measuring the differential photocurrent response to left circularly and right circularly polarized light after the formation of the DHS (Supplementary Figs. 36 and 38a). Illumination of the solution chamber consisting of DHS of ***S*-G** with left circularly polarized light exhibits a differential channel current of up to 1 μA at 2 V when compared with the photocurrent obtained after illumination with right circularly polarized light (Fig. 7d, e). This differential photoresponse translates to dissymmetry factor, or g_{factor} value as high as 0.55 at 2 V. Note that the g_{factor} increased from 0.3 at 0 V to a value of 0.55 at 2 V for ***S*-G** samples. Similarly, photocurrent response with chiral light was also measured for ***R*-G** solution, interestingly however it exhibited higher photoresponsivity towards right circularly polarized light and the magnitude of g_{factor} was obtained to be ~0.61 at 2 V (Supplementary Fig. 38b, c). Previous reports of organic molecules have shown g_{factor} nearly −0.113 for polymer blends[55], 0.054 for perylene diimide derivatives[58] and 0.1 for polymer and small molecule hybrids[57], all of which are lower than our measurement. Correspondingly, we observed a responsivity as high as 2 mA/W. More importantly, this enhanced selectivity towards chiral illumination brings out the potential utilization of these materials for chiral detection using programmable self-assembled structures.

In summary, we have demonstrated the non-covalent synthesis of higher-ordered chiral SP architectures having dendritic topology. We have observed that the secondary nucleation-elongation process involving 'growth on the surface' and 'growth from the surface' plays a crucial role in the formation of DHS. In the present case, we could synthesize DHS having a size of 0.4 mm^2. Moreover, these DHS show the best chiro-optical response to date in the solution phase with a magnitude of g_{factor} ~ 0.55–0.61 and a responsivity as high as 2 mA/W. Our results further indicate that the combination of both 'growth on the surface' and 'growth from the surface' secondary nucleation-elongation process can be further explored to synthesize more complex topologies of SPs, which are difficult to achieve only by one of these processes. It was observed that the secondary nucleation events are the key sources for the generation of toxic oligomeric species in the context of diseases[31,65]. On the other hand, secondary nucleation events are potentially useful for the non-covalent synthesis of higher-ordered supramolecular architectures[66], which are difficult to achieve solely via primary nucleation events. However, the same is challenging with small molecules as no rational design principles were available. Recent reports[33–35] and the results reported here shed light on molecular design principles and growth process, which would serve as a handy tool for the non-covalent synthesis of higher-ordered complex supramolecular architectures with high precision and selectivity for utilization in material science and biology.

Methods

DHS preparation

2 mg of ***S*-G**/***R*-G** was measured and transferred into a vial, and 2.634 mL of $CHCl_3$ was added to it to obtain a concentration of 1 mM, which is the stock solution. Concentration-dependent experiments of ***S*-G** by varying the concentration from 100 μM to 300 μM performed in $CHCl_3$ using UV-Vis absorption spectroscopy revealed a linear relation (Supplementary Fig. 39), indicating the absence of any preexisting aggregates of ***S*-G**/***R*-G** in $CHCl_3$ solution before the addition of IPA. From the 1 mM $CHCl_3$ stock solution, 90 μL was transferred into a vial, and 360 μL of $CHCl_3$ (good solvent) was added. To this, a further 2550 μL of IPA (poor solvent) was added and mixed well to make the whole volume 3 mL containing 30 μM of ***S*-G**/***R*-G** in 15% of $CHCl_3$ in IPA. These solutions were used for UV-Vis spectroscopy and CD measurements as such.

Sample preparation for FE-SEM and AFM measurements

FE-SEM images were collected using JEOL JIB4700F FIB-SEM, and AFM measurements were performed on Park Systems NX10 using NSG 30 tip with a scan rate of 0.3 Hz. Samples were prepared by spin-coating the solutions onto a silicon substrate at time intervals of 0 min., 15 min., 30 min. and 45 min. during evolution into DHS. Samples were dried by evaporation of solvent under vacuum at room temperature. For FE-SEM measurements, samples were sputtered with gold.

Device fabrication for electrical measurements

For the device fabrication, lateral Cr/Au electrodes were thermally evaporated (5/25 nm at 0.1 Å/s) onto a pre-cleaned glass substrate using the MiniLab 026 system by Moorfield Nanotechnology Limited, under a pressure of 10^{-6} mbar. A physical mask was employed during the evaporation process to create channels with lengths ranging from 1 μm to 3 μm and channel width of 0.7 to 0.78 cm on the substrate. Lithographically substrates with interdigitated electrodes were also utilized in some case. Notably both the device exhibit similar results. After that, a custom-designed 2 mL hollow chamber was securely attached over the channel using silicone adhesive as illustrated in Fig. 7a.

Time-dependent electrical current measurements and CPL detection

For each measurement, 1.5 mL of the prepared solution was transferred into the measurement chamber. Dual *I*–*V* sweeps were performed using a Keithley 2450 over a voltage range of −2 V to 2 V. The voltage value was chosen to ensure that it is smaller than the electrochemical window of the utilized solvents. To monitor the temporal evolution of the channel current the *I*–*V* sweeps were performed every 2 min. and continued for 50 min. For the chiro-optical measurement, circularly polarized light was generated using the set-up shown in Supplementary Fig. 36. After the formation of the DHS structure, *I*–*V* measurements were performed in the dark and then with left and right circularly polarized light illumination of $\lambda = 454$ nm. The g_{factor} was calculated using the expression: $\frac{I_L - I_R}{\frac{1}{2}(I_L + I_R)}$ and responsivity was estimated using the expression $R = \frac{I_{Ph} - I_D}{P_{input}}$; where I_{Ph} is current under illumination, I_D is current dark conditions and P_{input} (457 μW/m^2) is input power of the incident laser, I_L and I_R are the photocurrent upon illumination with left circularly and right circularly polarized light respectively.

Data availability

All data are available from the corresponding author upon request. The data generated in this study are provided in the Supplementary Information/Source Data file. Source data [https://doi.org/10.5281/zenodo.14090280] are provided in this paper.

References

1. Aida, T., Meijer, E. W. & Stupp, S. I. Functional supramolecular polymers. *Science* **335**, 813–817 (2012).
2. Peng, H. Q. et al. Supramolecular polymers: recent advances based on the types of underlying interactions. *Prog. Polym. Sci.* **137**, 101635 (2023).
3. Chen, H. & Stoddart, F. J. From molecular to supramolecular electronics. *Nat. Rev. Mater.* **6**, 804–828 (2021).
4. Jain, A. & George, S. J. New directions in supramolecular electronics. *Mater. Today* **18**, 206–214 (2015).
5. Moulin, E., Cid, J. J. & Giuseppone, N. Advances in supramolecular electronics – from randomly self-assembled nanostructures to addressable self-organized interconnects. *Adv. Mater.* **25**, 477–487 (2013).
6. Babu, S. S., Prasanthkumar, S. & Ajayaghosh, A. Self-assembled gelators for organic electronics. *Angew. Chem. Int. Ed.* **51**, 1766–1776 (2012).
7. Kazantsev, R. V. et al. Molecular control of internal crystallization and photocatalytic function in supramolecular nanostructures. *Chem* **4**, 1596–1608 (2018).
8. Rosso, C., Filippini, G. & Prato, M. Use of perylene diimides in synthetic photochemistry. *Eur. J. Org. Chem.* **8**, 1193–1200 (2021).
9. Goudar, S. H. et al. Supramolecular engineering of Ti3C2Tx MXene -perylene diimide hybrid electrodes for the pseudocapacitive electrochemical storage of calcium ions. *Small* **20**, 2309905 (2024).
10. Greef, T. F. A. D. D. et al. Supramolecular polymerization. *Chem. Rev.* **109**, 5687–5754 (2009).
11. Smulders, M. M. J. et al. How to distinguish isodesmic from cooperative supramolecular polymerisation. *Chem. Eur. J.* **16**, 362–367 (2010).
12. Kotha, S. et al. Cooperative supramolecular polymerization guided by dispersive interactions. *Chem. Asian J.* **17**, e202200494 (2022).
13. Wehner, M. & Würthner, F. Supramolecular polymerization through kinetic pathway control and living chain growth. *Nat. Rev. Chem.* **4**, 38–53 (2020).
14. Wagner, W., Wehner, M., Stepanenko, V. & Würthner, F. Supramolecular block copolymers by seeded living polymerization of perylene bisimides. *J. Am. Chem. Soc.* **141**, 12044–12054 (2019).
15. Sarkar, A. et al. Tricomponent supramolecular multiblock copolymers with tunable composition via sequential seeded growth. *Angew. Chem. Int. Ed.* **60**, 18209–18216 (2021).
16. Jarrett-Wilkins, C. et al. Living supramolecular polymerisation of perylene diimide amphiphiles by seeded growth under kinetic control. *Chem. Eur. J.* **24**, 15556–15565 (2018).
17. Ogi, S. et al. Living supramolecular polymerization realized through a biomimetic approach. *Nat. Chem.* **6**, 188–195 (2014).
18. Fukui, T. et al. Control over differentiation of a metastable supramolecular assembly in one and two dimensions. *Nat. Chem.* **9**, 493–499 (2017).
19. Yagai, S., Kitamoto, Y., Datta, S. & Adhikari, B. Supramolecular polymers capable of controlling their topology. *Acc. Chem. Res.* **52**, 1325–1335 (2019).
20. Tezuka, Y. Topological polymer chemistry designing complex macromolecular graph constructions. *Acc. Chem. Res.* **50**, 2661–2672 (2017).
21. Wu, Q. et al. Poly[n]Catenanes: synthesis of molecular interlocked chains. *Science* **358**, 1434–1439 (2017).
22. Cook, A. B. & Perrier, S. Branched and dendritic polymer architectures: functional nanomaterials for therapeutic delivery. *Adv. Funct. Mater.* **30**, 1901001 (2020).
23. Schroffenegger, M. et al. Polymer topology determines the formation of protein corona on core–shell nanoparticles. *ACS Nano* **14**, 12708–12718 (2020).
24. Miermans, C. A., Kusters, R. P., Hoogenraad, C. C. & Storm, C. Biophysical model of the role of actin remodeling on dendritic spine morphology. *PLoS One* **12**, e0170113 (2017).
25. Kasai, M., Asakura, S. & Oosawa, F. The cooperative nature of G-F transformation of actin. *Biochim. Biophys. Acta* **57**, 22–31 (1962).
26. MacFarlane, L. et al. Emerging applications for living crystallization-driven self-assembly. *Chem. Sci.* **12**, 4661–4682 (2021).
27. Wang, X. et al. Cylindrical block copolymer micelles and co-micelles of controlled length and architecture. *Science* **317**, 644–647 (2017).
28. Gädt, T. et al. Complex and hierarchical micelle architectures from diblock copolymers using living, crystallization-driven polymerizations. *Nat. Mater.* **8**, 144–150 (2009).
29. Jin, Z. et al. Two-dimensional living supramolecular polymerization: Improvement in edge roughness of supramolecular nanosheets by using a dummy monomer. *Chem. Eur. J.* **29**, e202302181 (2023).
30. Törnquist, M. et al. Secondary nucleation in amyloid formation. *Chem. Commun.* **54**, 8667–8684 (2018).
31. Cohen, S. I. A. et al. Proliferation of amyloid Aβ42 aggregates occurs through a secondary nucleation mechanism. *Proc. Natl. Acad. Sci.* **110**, 9758–9763 (2013).
32. Laishram, R. et al. Secondary nucleation-triggered physical cross-links and tunable stiffness in seeded supramolecular hydrogels. *J. Am. Chem. Soc.* **144**, 11306–11315 (2022).
33. Datta, S. et al. Self-assembled poly-catenanes from supramolecular toroidal building blocks. *Nature* **583**, 400–405 (2020).
34. Sasaki, N. et al. Supramolecular double-stranded archimedean spirals and concentric toroids. *Nat. Commun.* **11**, 3578 (2020).
35. Kotha, S. et al. Noncovalent synthesis of homo and hetero-architectures of supramolecular polymers via secondary nucleation. *Nat. Commun.* **15**, 3672 (2024).
36. García, F., Gómez, R. & Sánchez, L. Chiral supramolecular polymers. *Chem. Soc. Rev.* **52**, 7524–7548 (2023).
37. Liu, M., Zhang, L. & Wang, T. Supramolecular chirality in self-assembled Systems. *Chem. Rev.* **115**, 7304–7397 (2015).
38. Xu, L. et al. Crystallization-driven asymmetric helical assembly of conjugated block copolymers and the aggregation induced white-light emission and circularly polarized luminescence. *Angew. Chem. Int. Ed.* **59**, 16675–16682 (2020).
39. Wang, C., Xu, L., Zhou, L., Liu, N. & Wu, Z. Q. Asymmetric living supramolecular polymerization: precise fabrication of one-handed helical supramolecular polymers. *Angew. Chem. Int. Ed.* **61**, e202207028 (2022).
40. Liu, N., Gao, R. T. & Wu, Z. Q. Helix-induced asymmetric self-assembly of π-conjugated block copolymers: from controlled syntheses to distinct properties. *Acc. Chem. Res.* **56**, 2954–2967 (2023).
41. Gao, R. T. et al. One-pot asymmetric living copolymerization-induced chiral self-assemblies and circularly polarized luminescence. *Chem. Sci.* **15**, 2946–2953 (2024).
42. Sang, Y. et al. Circularly polarized luminescence in nanoassemblies: generation, amplification, and application. *Adv. Mater.* **32**, 1900110 (2020).
43. Zimbron, J. M. et al. Real-time control of the enantioselectivity of a supramolecular catalyst allows selecting the configuration of consecutively formed stereogenic centers. *Angew. Chem. Int. Ed.* **56**, 14016–14019 (2017).
44. Dou, X. et al. Supramolecular hydrogels with tunable chirality for promising biomedical applications. *Acc. Chem. Res.* **53**, 852–862 (2020).
45. Mondal, A. K. et al. Spin filtering in supramolecular polymers assembled from achiral monomers mediated by chiral solvents. *J. Am. Chem. Soc.* **143**, 7189–7195 (2021).

46. Lafleur, R. P. M. at al. Supramolecular double helices from small C3-symmetrical molecules aggregated in water. *J. Am. Chem. Soc.* **142**, 17644–17652 (2020).
47. Hifsudheen, M. et al. The Helix to super-helix transition in the self-assembly of π-systems: superseding of molecular chirality at hierarchical level. *Angew. Chem. Int. Ed.* **56**, 12634–12638 (2017).
48. Li, H. & Chen, L. Three-level hierarchical self-assembly of azobenzene conjugated phenylalanines into superhelical nanostructures with light-switchable helicity. *Org. Chem. Front.* **9**, 6240–6246 (2022).
49. Liu, Y. et al. Emergent self-assembly pathways to multidimensional hierarchical assemblies using a hetero-seeding approach. *Chem. Eur. J.* **25**, 13484–13490 (2019).
50. Sun, B. et al. Homochiral porous nanosheets for enantiomer sieving. *Nat. Mater.* **17**, 599–604 (2018).
51. Du, C. et al. Hierarchically self-sssembled homochiral helical microtoroids. *Nat. Nanotechnol.* **17**, 1294–1302 (2022).
52. Taylor, K. C. et al. Skip residues modulate the structural properties of the myosin rod and guide thick filament assembly. *Proc. Natl. Acad. Sci.* **112**, E3806–E3815 (2015).
53. Sarkar, S. et al. Stereoselective primary and secondary nucleation events in multicomponent seeded supramolecular polymerization. *J. Am. Chem. Soc.* **143**, 11777–11787 (2021).
54. Sarkar, S., Laishram, R., Deb, D. & George, S. J. Controlled non-covalent synthesis of secondary supramolecular polymers. *J. Am. Chem. Soc.* **145**, 22009–22018 (2023).
55. Wan, L. et al. Sensitive near-infrared circularly polarized light detection via non-fullerene acceptor blends. *Nat. Photonics* **17**, 649–655 (2023).
56. Yang, Y., Correa da Costa, R., Fuchter, M. J. & Campbell, A. J. Circularly polarized light detection by a chiral organic semiconductor transistor. *Nat. Photonics* **7**, 634–638 (2013).
57. Kim, N. Y. et al. Chiroptical-conjugated polymer/chiral small molecule hybrid thin films for circularly polarized light-detecting heterojunction devices. *Adv. Funct. Mater.* **29**, 1808668–1808678 (2019).
58. Zhang, L. et al. π-Extended perylene diimide double-heterohelicenes as ambipolar organic semiconductors for broadband circularly polarized light detection. *Nat. Commun.* **12**, 142 (2021).
59. Langhals, H. & Blanke, P. An Approach to novel NIR dyes utilising α-Effect donor groups. *Dyes Pigm.* **59**, 109–116 (2003).
60. Würthner, F. et al. Perylene bisimide dye assemblies as archetype functional supramolecular materials. *Chem. Rev.* **116**, 962–1052 (2016).
61. Kotha, S. et al. Pathway selection in temporal evolution of supramolecular polymers of ionic π-systems: amphiphilic organic solvent dictates the fate of water. *Chem. Eur. J.* **30**, e202303813 (2024).
62. Meisl, G. et al. Molecular mechanisms of protein aggregation from global fitting of kinetic models. *Nat. Protoc.* **11**, 252–272 (2016).
63. Zimmermann, M. R. et al. Mechanism of secondary nucleation at the single fibril level from direct observations of Aβ42 aggregation. *J. Am. Chem. Soc.* **143**, 16621–16629 (2021).
64. Zhang, Y. et al. Dendritic micelles with controlled branching and sensor applications. *J. Am. Chem. Soc.* **143**, 5805–5814 (2021).
65. Gracia, P., Camino, J. D., Volpicelli-Daley, L. & Cremades, N. Multiplicity of a-synuclein aggregated species and their possible roles in disease. *Int. J. Mol. Sci.* **21**, 8043 (2020).
66. Datta, S., Takahashi, S. & Yagai, S. Nanoengineering of curved supramolecular polymers: toward single-chain mesoscale materials. *Acc. Mater. Res.* **3**, 259–271 (2022).

Acknowledgements

K.V.R. acknowledge the Core Research Grant (SERB-CRG) from the Science and Engineering Research Board (CRG/2023/001575) for financial support. S.K.R. and K.V.R. acknowledge Core Research Grant (SERB-CRG) from the Science and Engineering Research Board (Grant number CRG/2022/006457) for financial support. S.R.P. acknowledges the scholarship support from MOE, the government of India, India. D.S. acknowledges the scholarship support from MOE, the government of India, India. A.C.Y. thanks the MOE, India, for the Prime Minister research fellowship. We thank professor Subi J. George from JNCASR, Bangalore, for MALDI-TOF measurements. S.P.S. acknowledges funding support from Intensification of Research in High Priority Areas (IRHPA) funding from the Science and Engineering Research Board (IPA/2021/000096), funding from the Department of Atomic Energy (DAE), Government of India through RIN-4001. U.P. and D.I.S. acknowledge funding support from DAE through the Disha Fellowship. R.S. thanks UGC, India for the Senior Research Fellowship.

Author contributions

K.V.R. conceived the idea. S.R.P. performed all the experiments except electrical conductivity measurements and theoretical calculations. D.S. and A.C.Y. co-performed some of the experiments with S.R.P. U.P., D.I.S., and C.M. performed the electrical conductivity measurements of the self-assembled structures along with the chiro-optical measurements under the guidance of S.P.S. S.P.S. conceived the idea related to the electrical measurements and chiro-optical measurements. R.S. and S.K.R. carried out the MD simulations. K.V.R. and S.P.S. supervised the overall project. All the authors discussed the results and contributed to the manuscript writing. The manuscript was written through the contributions of all authors. All authors have given approval to the final version of the manuscript.

Competing interests

The authors declare no competing interests.

Additional information

Supplementary information The online version contains supplementary material available at https://doi.org/10.1038/s41467-024-55107-y.

Correspondence and requests for materials should be addressed to Satyaprasad P. Senanayak or Kotagiri Venkata Rao.

Peer review information *Nature Communications* thanks Jun Guan, Michel Rickhaus and the other, anonymous, reviewer(s) for their contribution to the peer review of this work. A peer review file is available.